Localization-delocalization transition of the instantaneous normal modes of liquid water

Ban-Chiech Huang[1] and Cheng-Hung Chang[1,2]

[1]*Institute of Physics, National Chiao Tung University, Hsinchu 300, Taiwan*
[2]*National Center for Theoretical Sciences, Hsinchu 300, Taiwan*

Despite the fact that the localization-delocalization transition (LDT) widely exists in wave systems, quantitative studies on its critical and multifractal properties are mainly focused on solids. In this work, these properties are investigated on the vibrational motions of liquid water. Simulations of up to 18 000 molecules on the flexible extended simple point charge water model provide nearly 10^6 instantaneous normal modes. They are shown to undergo an LDT close to the translational transition and exhibit multifractal fluctuations while approaching the LDT. In combination with finite-size scaling, multifractal analysis predicts the critical frequency $\mathrm{Im}(\omega_c) \approx -131.6 \ \mathrm{cm}^{-1}$ for unstable modes at room temperature. The estimated critical exponent $\nu \approx 1.60$ is close to those of other calculated systems in the same Wigner-Dyson class. At the LDT, the fractal spectrum $f(\alpha)$ and the most probable local vibrational intensity $\alpha_{mc} \approx 4.04$ coincide with those of the Anderson model, which might be additional universal properties of LDT in more general wave systems. The results extend the validity of the multifractal scaling approach beyond Andersonian systems to a Hessian system.

I. INTRODUCTION

The localization-delocalization transition (LDT) is a phase transition of waves from localized to delocalized (extended) phases, as parameters characterizing these waves are varied through certain critical values. The concept of LDT has been around for more than 50 years, dating back to Anderson's seminal work [1–5]. It was originally proposed to account for the disorder-induced metal-insulator transition. According to Anderson's initial model, an extended wave function of an electron will undergo an LDT into a localized one when the disorder strength of the Hamiltonian rises to a critical value. The abrupt inhibition of wave transport is caused by the interference of multiple scattered waves [6]. Since interference is a fundamental property of waves, the LDT is expected to exist widely in nature. In addition to matter waves, this transition has been found in a variety of classical systems [3,7–15]. Among others, the vibration of liquids belongs to an essential category [16–23]. These soft matter systems are distinguished from the Anderson model (AM) in that their constituent particles transmitting waves can ceaselessly exchange positions and diffuse. Thus their localized waves can only exist instantaneously and do not have a time-independent spatial exponential decay like that in disordered solids.

The instantaneous normal mode (INM) analysis is an instrumental tool for understanding the eigendeviations of an instantaneous configuration of particles (see Sec. II B). The INM spectra can be used to clarify the liquid dynamics observed in infrared and vibrational Raman spectra [21,22,24] and reveal various liquid behaviors [17,19–23,25–30]. At low temperatures, the vanishing unstable delocalized modes in the INM spectrum are related to the liquid-glass transition [12]. At ambient temperatures, the imaginary part of the INM spectrum carries the information of barrier crossing and diffusion in fluids [26–30]. This issue brings about a long-standing discussion concerning whether INMs can explicitly determine the diffusion constant [31–33]. A recent study supports that conjecture by using the Adam-Gibbs theory to connect the diffusion constant with the delocalized unstable

INMs classified by the position of the LDT [19]. These studies highlight the intriguing relation between the LDT and the transport property of a soft matter system, in analogy to the similar relation well known in Anderson localization in solid state physics.

To locate the LDT position of liquid vibrations, the participation ratio p might be the first characteristic one would think of. In a rigid [20] and a flexible [21] water model, the fast decline of p with the increasing INM frequency was regarded as a sign for the area where the LDT occurs. In a soft sphere system at a supercooled temperature, the LDT position was roughly selected as being located in the frequency area whose vibrational modes have $p \approx 0.35$–0.38 in a system of 500 particles [12]. These values were later adopted to discuss other liquid properties such as diffusion [31]. Generally, the LDT locations of liquids known at that time were much less precise than those estimated in solids [34,35]. The high precision achieved in the latter was not ascribed to particularly competent methods, but to the usage of the scaling invariance property of the LDT. Although this property had also been noticed in an early discussion about the LDT of a revised transferable intermolecular potential water model [20], it appeared only as a remark in that work. A later study did use this property [12], which, however, only ended up with a roughly estimated LDT region, partly due to the insufficient size of the studied system consisting of merely 1024 particles. Until recently, the scaling invariance property was seriously considered in the studies of liquid LDT [19,36]. This advance has largely improved the accuracy of the extracted LDT locations of liquids and allowed us to explore their critical and multifractal behaviors.

A fractal has an intimate connection with phase transitions, which can be readily illustrated in several percolating network related problems [37–39]. At the Anderson transition, Aoki proposed that geometry to explain why the extended electron matter waves have a vanishing participation ratio while approaching the LDT [40]. This idea turns out to be the currently known multifractal fluctuations of critical modes, in

which local vibrations of different magnitudes have different fractal dimensions (see Sec. II C for more details). Owing to the same argument, a multifractal is expected to appear in general wave systems. This unique feature offers several candidates for scaling quantities for LDT determination. Examples include the position of the maximum α_m of the distribution $P(\alpha)$ of the local Hölder exponent α [17,41], the position of the maximum of the fractal spectrum $f(\alpha)$, the information dimension [35,38], and several multifractal exponents such as the generalized singularity strength $\widetilde{\alpha}_q$ [42,43]. The applicability of these scaling quantities is validated by the consistent results obtained from different methods over different systems in the same universality class [5]. For instance, the critical points and exponents of the three-dimensional (3D) AM extracted from the quantities $\widetilde{\alpha}_q$ and α_m [43], the level spacing [34], the level number variance [44], and the transfer matrix [45] are close to one another. The critical exponents of the 3D AM estimated by multifractal exponents [42,43] agree well with that of a truncated Lennard-Jones liquid (TLJL) evaluated by the level spacing statistics [36] and that of the disordered lattices with random mass or spring distributions (DLMS) calculated by the transfer matrix [14,15]. Among all approaches, the multifractal finite-size scaling (MFSS) is a recently proposed tool, which combines multifractal analysis with finite-size scaling [42,43]. This approach is constructed on the wave functions of the explored system and is particularly valuable for experiments where local wave-function amplitudes are accessible. Its application to the 3D AM has provided accurate critical properties; however, it has not been applied and validated elsewhere beyond the 3D AM.

In this work we used this multifractal scaling concept to explore liquid water, which was simulated by a flexible extended simple point charge (FSPC/E) model [46]. We demonstrated the multifractal fluctuations of the critical INMs of the FSPC/E model through the characteristic shape of $f(\alpha)$ and showed the connection between the LDT and the translational transition. We utilized the size invariant α_m and $\widetilde{\alpha}_q$ to extract several critical parameters of unstable INMs, including the critical frequency $\mathrm{Im}(\omega_c) \approx -131.6$ cm^{-1} and the critical exponent $\nu \approx 1.60$. The results offer a soft condensed matter system with an explicitly calculated ν. This value is close to those of the 3D AM, TLJL, DLMS, and quasiperiodic atomic kicked rotors (QARs) [47], all of which belong to the same symmetry class [5]. The findings not only unravel the LDT properties of liquid water, but also validate the multifractal scaling approach in a non-Andersonian Hessian system.

The paper is organized as follows. In Sec. II we introduce the FSPC/E water model and the molecular dynamics approach used in this work and sketch the INM analysis, the multifractal analysis, and the finite-size scaling theory. In Sec. III we demonstrate the vibrational density of states (DOS) of INMs and its translational, rotational, and stretching projectors and show the correspondence between the translational transition and the LDT. Then we focus on the INMs of imaginary frequencies and apply the multifractal scaling to calculate their critical parameters, including the critical frequency, critical exponent, and irrelevant exponent. In Sec. IV we discuss the obtained results and several related open questions. A summary is given in Sec. V. Note that the position of the LDT has several synonymous names, such as the

critical point in Anderson transitions, the mobility edge in lattice vibrations, and the critical frequency in the vibrations of liquids.

II. METHODS

A. Molecular dynamics method

The potential of the FSPC/E model,

$$U = U_{\mathrm{bond}} + U_{\mathrm{bend}} + U_{\mathrm{Coulomb}} + U_{\mathrm{LJ}}, \tag{1}$$

consists of four contributions. The bonding potential $U_{\mathrm{bond}} = \sum_i k_b (r_i - \bar{r})^2 + k_c k_b (r_i - \bar{r})^3$ sums over the O-H bonds in all molecules, with r_i the length of the ith bond, $\bar{r} = 0.1$ nm the bond length of the minimum U_{bond}, $k_b = 229\,008$ kJ nm^{-2} mol^{-1} the harmonic force constant, and $k_c = -1.65$ nm^{-1} the anharmonic coefficient. The bending potential $U_{\mathrm{bend}} = \sum_i k_a (\theta_i - \bar{\theta})^2$ counts the potential energy stored in the H-O-H angles of all water molecules, with the molecule index i, the proportional constant $k_a = 208.78$ kJ mol^{-1} rad^{-2}, and the bond angle $\bar{\theta} = 109.43°$ of the minimum U_{bend} [46]. The Coulomb potential between all charges in the system is effectively described by the reaction field [48]

$$U_{\mathrm{Coulomb}} = \sum_{i>j} f \frac{q_i q_j}{\varepsilon_r} \left(\frac{1}{r_{ij}} + k_{rf} r_{ij}^2 - C_{rf} \right) \tag{2}$$

Here $f = 138.935\,485$ kJ mol^{-1} nm e^{-2}, i and j (with $i > j$) run over all oxygen and hydrogen atoms at different molecules, r_{ij} is the distance between these atoms, and q_i and q_j can be either the partial charge $q_{\mathrm{O}} = -0.8476$ of the oxygen atom or the partial charge $q_{\mathrm{H}} = 0.4238$ of the hydrogen atom. Furthermore, $k_{rf} = (\varepsilon_{rf} - \varepsilon_r)/[r_c^3(2\varepsilon_{rf} + \varepsilon_r)]$ and $C_{rf} = 3\varepsilon_{rf}/[r_c(2\varepsilon_{rf} + \varepsilon_r)]$, with the frequently used cutoff length $r_c = 0.9$ nm, where $\varepsilon_r = 1$ and $\varepsilon_{rf} = 78$ are the relative dielectric constants in vacuum and water, respectively. Using this reaction field, the electrostatic interactions are calculated explicitly up to the cutoff distance r_c, beyond which a uniform dielectric constant ε_{rf} is assumed. The Lennard-Jones potential

$$U_{\mathrm{LJ}} = \sum_i \frac{C_{12}}{r_i^{12}} - \frac{C_6}{r_i^6} \tag{3}$$

describes the interactions between all oxygen-oxygen pairs, with $C_6 = 2.6171 \times 10^{-3}$ kJ mol^{-1} nm^6, $C_{12} = 2.6331 \times 10^{-6}$ kJ mol^{-1} nm^{12}, and r_i the distance between the two atoms in the ith pair. This FSPC/E model is distinguished from the common rigid model SPC/E in that it allows the stretching of the O-H bond and the bending of the H-O-H angle [49].

All molecular dynamics simulations were carried out using the leapfrog algorithm in the GROMACS 4.5 simulation suite under constant NVT [48], with an integration time step of 0.1 fs, where constraints such as the SHAKE, SETTLE, or LINCS algorithm were removed. The water density was set to $\rho = 1$ g/cm^3 and the temperature was held at 298 K by the velocity-rescaling method. The system will reach equilibrium after 1 ns of simulation and the subsequent water configurations are recorded every picosecond to build up an ensemble of water configurations for INM analysis.

B. Instantaneous normal mode analysis

Each instantaneous water configuration has a potential U, as defined in Eq. (1), which leads to instantaneous vibrations and INMs. These modes are the eigenvectors of the Hessian matrix generated by the second derivative of U. For a system of N flexible water molecules, the $9N$-dimensional atomic coordinate $e_{i\alpha\mu}$ describes the μth component of the position of the αth atom in the ith molecule, where $\mu \in \{x,y,z\}$, $i \in \{1,2,\ldots,N\}$, and $\alpha = 1, 2$, and 3 represent the first and second hydrogen atoms and the oxygen atom, respectively. The mass-weighted coordinate is defined as $\eta_{i\alpha\mu} = \sqrt{m_\alpha}\, e_{i\alpha\mu}$, where m_α stands for the mass of the αth atom in a molecule. The Hessian matrix has the matrix entries

$$D_{i\alpha\mu;j\beta\nu} = \frac{\partial^2 U}{\partial \eta_{i\alpha\mu} \partial \eta_{j\beta\nu}}, \qquad (4)$$

in units of squared frequency. If ω^2 is an eigenvalue of that matrix, ω is the vibrational frequency of the instantaneous water configuration. The eigenvector ζ of ω^2 can be expressed in terms of the unit vectors $\hat{\eta}_{i\alpha\mu}$ along the coordinates $\eta_{i\alpha\mu}$,

$$\zeta = \sum_{i=1}^{N} \sum_{\alpha=1}^{3} \sum_{\mu \in \{x,y,z\}} c_{i\alpha\mu} \hat{\eta}_{i\alpha\mu}, \qquad (5)$$

where $c_{i\alpha\mu}$ is the component of ζ in the $\hat{\eta}_{i\alpha\mu}$ direction and the normalization condition for ζ requires

$$\sum_{i,\alpha,\mu} |c_{i\alpha\mu}|^2 = 1. \qquad (6)$$

The INM DOS is given by

$$D(\omega) = \frac{1}{9N} \left\langle \sum_{s=1}^{9N} \delta(\omega - \omega_s) \right\rangle, \qquad (7)$$

where $\delta(x)$ is the Dirac delta function. Here the sum runs over all INM frequencies ω_s of an instantaneous configuration and $\langle\cdot\rangle$ denotes an ensemble average over all accessible configurations.

If the atom configuration is quenched to a local minimum of the potential energy surface (PES) [50], it will return to the minimum under any infinitesimal perturbation. This minimum has a positive curvature and its Hessian matrix has only positive eigenvalues $\omega^2 > 0$. If the system is at normal temperatures, the atom configuration is in general not at a PES minimum. Hence it may not be restored to its initial configuration under a perturbation. The Hessian matrix may accordingly contain some negative eigenvalues $\omega^2 < 0$, which give pure imaginary ω. The real (imaginary) frequencies and their modes are referred to as the stable (unstable) frequencies and modes, respectively. The densities of the real (imaginary) frequencies are conventionally plotted on the positive (negative) axis of the INM spectrum. In the following studies, the JADAMILU package [51] was used to solve the eigenvectors of the Hessian matrices whose frequencies lie within the observation windows Σ (see Sec. III B).

For a rigid water model of N molecules, the system potential U can be expressed in terms of $3N$ pure translational and $3N$ pure rotational coordinates [20]. Under this expression, the $c_{i\alpha\mu}$ in Eq. (5) is relabeled as $c_{\sigma k}$, where $\sigma = 1$ and 2 denote the translational and rotational components, respectively. The

normalization condition on a $6N$-dimensional INM of such system requires $\sum_{\sigma=1}^{2} \sum_{k=1}^{3N} |c_{\sigma k}|^2 = 1$. The translational and rotational projectors are the partial sums $P^{\text{trans}} = \sum_{k=1}^{3N} |c_{1k}|^2$ and $P^{\text{rot}} = \sum_{k=1}^{3N} |c_{2k}|^2$, respectively, in that condition. For a flexible water model such as FSPC/E, we can express its U in terms of $3N$ translational coordinates for the centers of mass (c.m.) in the N water molecules, as well as $4N$ and $2N$ coordinates for the internal rotational and stretching degrees of freedom in the molecules, respectively. Following the same strategy as used in the rigid water [52], a $9N$-dimensional INM of FSPC/E will have the translational, rotational, and stretching projectors $P^{\text{trans}} = \sum_{k=1}^{3N} |c_{1k}|^2$, $P^{\text{rot}} = \sum_{k=1}^{4N} |c_{2k}|^2$, and $P^{\text{stretch}} = \sum_{k=1}^{2N} |c_{3k}|^2$, respectively. Furnishing the projectors with a subscript s to denote the sth INM, the translational, rotational, and stretching DOSs are

$$D^\lambda(\omega) = \frac{1}{9N} \left\langle \sum_{s=1}^{9N} \delta(\omega - \omega_s) P_s^\lambda \right\rangle, \qquad (8)$$

where λ stands for the abbreviations trans, rot, or stretch. In practice, the c.m. of a water molecule is rather close to the position of its oxygen atom because 8/9 of the mass of the molecule lies in that atom. Regarding the oxygen position approximately as the c.m. of the molecule, the rotational and stretching degrees of freedom inside the molecule can be represented by the motions of the two hydrogen atoms relative to the oxygen atom. Thus the rotational and stretching components $c_{\sigma k}$ can be calculated by projecting the INM onto the tangential and normal unit vectors $\vec{T}_i$ and $\vec{S}_i$, in the inset of Fig. 1, where $i = 1$ and 2 represent the first and second hydrogen atoms, respectively.
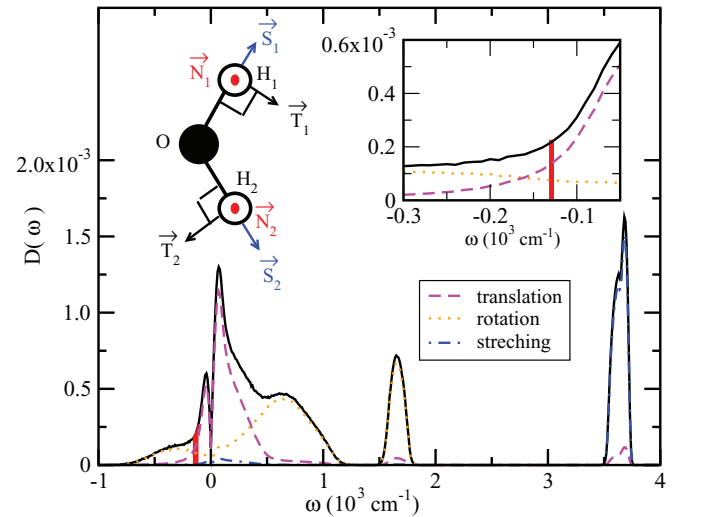

FIG. 1. (Color online) Vibrational DOS of INMs (black solid curve) partitioned into translational, rotational, and stretching DOSs of INMs, depicted by the pink dashed, orange dotted, and blue dash-dotted curves, respectively. In the inset, the LDT area (red stripe) of the unstable modes is magnified where the positions of the LDT and the translational transition are clearly seen. In the plot left of the inset, $\vec{T}_i$ and $\vec{S}_i$ denote the tangential and normal unit vectors on the ith hydrogen atom of a water molecule and $\vec{N}_i$ is its unit vector perpendicular to the molecular plane.

C. Multifractal analysis

The application of multifractal analysis usually starts with dividing the system into boxes and assigning a measure $\mu_i = \sum_{j\in\text{box } i} |\psi_j|^2$ to count the local squared amplitudes $|\psi_j|^2$ of a wave ψ at all sites j in the ith box. The function ψ is assumed to be normalized in the following discussions. Given a box with the measured value μ, the local Hölder exponent

$$\alpha = -\ln\mu/\ln L \qquad (9)$$

is a rescaled local intensity of the wave in that box. Here $L = L_{\text{sys}}/l$ is a dimensionless length of the system, with L_{sys} and l the system and box sizes of normal length units, respectively. The larger the μ, the smaller the value of α is. The distribution $P(\alpha)$ is the probability density function (PDF) of finding a box having intensity α. This function can be approximated by the histogram $\Delta N_\alpha/\bar{N}$, when the total box number $\bar{N}$ is large, where ΔN_α is the number of boxes with intensity α. The position of the maximum PDF α_m is the most probable intensity that can be found in the wave. Generally, the boxes of intensity α have an α-dependent fractal dimension $f(\alpha)$ and ΔN_α is scaled with the system length L by $\Delta N_\alpha \sim L^{f(\alpha)}$.

The generalized inverse participation ratio is a measure that can characterize the uniformity of a fluctuating wave. This ratio is defined as

$$R_q = \sum_{i=1}^{\bar{N}} \mu_i^q, \qquad (10)$$

where the sum runs over all boxes. For $q = 2$, R_q is the conventional inverse participation ratio, which is 1 for a completely localized wave and tends to 0 for a completely uniform wave. For $q > 0$ and $q < 0$, the boxes with large and small intensities, respectively, are more weighted and contribute more to R_q. In the thermodynamic limit, the ensemble average of R_q, over all accessible disorder configurations, behaves asymptotically as

$$\langle R_q \rangle \sim L^{-\tau_q}, \qquad (11)$$

where τ_q is the mass exponent. For localized, delocalized, and multifractal modes, the exponent takes the values $\tau_q = 0$, $d(q-1)$, and $D_q(q-1) = d(q-1) + \Delta_q$, respectively, with the anomalous dimension Δ_q. This exponent is related to the singularity spectrum $f_q \equiv f(\alpha_q)$ of the singularity strength α_q through the Legendre transformation [37]

$$f_q = q\alpha_q - \tau_q \quad \text{for} \quad \alpha_q = d\tau_q/dq. \qquad (12)$$

The quantities τ_q, Δ_q, and α_q are the multifractal exponents.

The most thoroughly studied multifractal behaviors of the LDT might be those of the AM. Several numerical and theoretical results of this model have rendered it to be a paradigm for understanding the LDT of general wave systems [4,5]. When the energy or disorder strength of the AM is varied through the critical point, the system undergoes a transition from the metallic phase with delocalized electric wave functions to the insulating phase with localized electric wave functions. A localized wave will decay exponentially as

$$|\psi(\mathbf{r})|^2 \sim \exp(-|\mathbf{r} - \mathbf{r}_0|/\xi) \qquad (13)$$

with respect to its center $\mathbf{r}_0$, where ξ is the localization length of that wave. On the insulating side (say, $E < E_c$),

the localization length scales with

$$\xi \sim (E_c - E)^{-\nu}, \qquad (14)$$

when the system energy E approaches the critical point E_c, where ν is the critical exponent of the localization length. If the system size L is finite, ξ will exceed L when E lies in an energy region Λ around E_c, termed the critical region. A wave function is a critical mode if its E is in Λ and a delocalized (localized) mode if its E is smaller (larger) than all values in Λ. The localized, delocalized, and critical modes have $\tau_q = 0$, $d(q-1)$, and $D_q(q-1)$, respectively. In the thermodynamic limit, the critical region Λ shrinks to the critical point E_c.

The fractal dimension $f(\alpha)$ is a characteristic property of multifractals [38]. A wave is multifractal if and only if its $f(\alpha)$ versus $\ln\lambda$ can be fitted by straight lines [35], where $\lambda = 1/L$.[1] Theoretical studies have proved that at the critical point, $f(\alpha)$ should follow a symmetric relation $f(2d - \alpha) = f(\alpha) + d - \alpha$ for systems in the three Wigner-Dyson classes [53] and other unconventional symmetry classes [54]. Numerically, this relation has been confirmed in the AM [43,55,56] and the TLJL [17]. In fact, the $f(\alpha)$ of currently known systems not only follow the above symmetry, but also exhibit a common bell shape [10,17,41,57]. In this work we shall inspect whether the $f(\alpha)$ of the FSPC/E water model also shares the same characteristic shape. To calculate $f(\alpha)$, we can use the conventional box-counting procedure or the relation $P(\alpha) \sim L^{f(\alpha)-d}$, owing to the asymptotic behaviors $\Delta N_\alpha \sim L^{f(\alpha)}$, $\bar{N} \sim L^d$, and $P(\alpha) \approx \Delta N_\alpha/\bar{N}$ for large L. More explicitly, one can argue and numerically verify that

$$P(\alpha) = P(\bar{\alpha})L^{f(\alpha)-d}, \qquad (15)$$

where the position of the maximum $\bar{\alpha}$ of $f(\alpha)$ is equal to the position of the maximum α_m of $P(\alpha)$ [41]. Since the critical modes of the two completely distinct systems, the 3D AM [41] and the TLJL [17], have almost the same value $\alpha_m \approx 4.0$, it raises the question of whether this value could serve as a criterion for determining the LDT location of general systems. It looks feasible for systems whose critical modes have the same $f(\alpha)$ because Eq. (15) infers that the same $f(\alpha)$ will lead to the same α_m. This gives another motivation to compare the $f(\alpha)$ of different systems.

As mentioned in Sec. I, several multifractal variables may be used as scaling quantities for determining the critical point. However, contradictorily, truly multifractal behaviors only appear at the critical point, which has to be solved before multifractals can be discussed. Recently, the MFSS theory overcomes this obstacle and extends the multifractal analysis from the critical point to the vicinity of that point. It admits a simultaneous estimation on the critical parameters and multifractal exponents, without knowing the precise location of the critical point beforehand. The MFSS theory begins with defining the generalized mass exponent [43]

$$\widetilde{\tau}_q := \frac{\ln\langle R_q \rangle}{\ln\lambda} \qquad (16)$$

---

[1]In Ref. [43], $\lambda = l/L$, where L is the system size measured in terms of the lattice constant and l is supposed to be in the same units. In this work, $\lambda = 1/L$, where L is the dimensionless system size in the same units as box size. Thus both λ have the same meaning.

throughout the critical region around the critical point. In combination with the scaling concept, the generalized anomalous dimension $\widetilde{\Delta}_q$, singularity spectrum $\widetilde{f}_q$, and singularity strength $\widetilde{\alpha}_q$ can be derived, where the latter two are related in analogy to Eq. (12),

$$\widetilde{f}_q = q\widetilde{\alpha}_q - \widetilde{\tau}_q, \quad \widetilde{\alpha}_q = d\widetilde{\tau}_q/dq. \tag{17}$$

Alternatively, one can define $\widetilde{\alpha}_q$ through the PDF $P(\alpha)$,

$$\widetilde{\alpha}_q = \frac{\int_0^\infty \alpha \lambda^{q\alpha} P(\alpha) d\alpha}{\int_0^\infty \lambda^{q\alpha} P(\alpha) d\alpha}, \tag{18}$$

which is a modified first moment of α. The tildes on $\widetilde{\tau}_q$, $\widetilde{\Delta}_q$, and $\widetilde{\alpha}_q$ emphasize that the validity of these quantities is beyond the critical point [43]. Although the local Hölder exponent α in $P(\alpha)$ is not restricted to the critical point, for simplicity, we do not add a tilde to emphasize it anymore. The quantities $\widetilde{\tau}_q$, $\widetilde{\Delta}_q$, and $\widetilde{\alpha}_q$ will converge to τ_q, Δ_q, and α_q at the critical point in the limit $\lambda \to 0$ [43]. All of them are candidates for scaling quantities in the finite-size scaling approach. At first glance, this statement seems to be trivial because all these quantities are related to $P(\alpha)$. They would be automatically size invariant at the critical point if the shape of $P(\alpha)$ were also invariant at that point. Unfortunately, it is true only when λ is fixed during the size change [41]. For general cases with a varying λ like in the following discussion, what is invariant in $P(\alpha)$ is not its shape, but the position of its maximum, as indicated by Eq. (15). Thus scaling approaches using $\widetilde{\tau}_q$, $\widetilde{\Delta}_q$, and $\widetilde{\alpha}_q$ are worthy of individual studies. Recently, the LDT of the 3D AM has been studied by the MFSS theory [43], where the critical parameters estimated from different q are consistent with one another.

D. Finite-size scaling theory

The multifractal quantities mentioned above will be scaled with system size to evaluate the critical parameters, based on the general belief that the LDT is a second-order phase transition [3]. According to the one-parameter scaling hypothesis [58], a localization transition at the critical point w_c can be characterized by the divergence of the localization (correlation) length

$$\xi(w) = |\chi(W)|^{-\nu}. \tag{19}$$

Here $\chi(W)$ is generally a nonlinear function of $W = (w - w_c)/w_c$, where ν denotes the critical exponent of the localization length and w in the LDT study is commonly the energy, disorder strength, or frequency. The ξ of the AM in Eq. (14) is a special case of Eq. (19), whose χ is a linear function of energy. Near the critical point, a multifractal quantity X, such as the above-mentioned $\widetilde{\tau}_q$, $\widetilde{\Delta}_q$, and $\widetilde{\alpha}_q$, can be scaled by a function g through

$$X = X_0 + \frac{1}{\ln L} g(\chi_r L^{1/\nu}, \chi_i L^y), \tag{20}$$

where χ_r and χ_i are the relevant and irrelevant scaling variables, respectively, X_0 is the value of X at the critical point, and $y < 0$ is the irrelevant exponent, which takes care of the irrelevant shift [45]. The function g can be

approximated by

$$g = \widetilde{g}_0(\chi_r L^{1/\nu}) + \chi_i L^y \widetilde{g}_1(\chi_r L^{1/\nu}) + \chi_i L^{2y} \widetilde{g}_2(\chi_r L^{1/\nu}), \tag{21}$$

where the series $\widetilde{g}_0(Z) = \sum_{j=0}^{n_0} a_{0j} Z^j$, $\widetilde{g}_1(Z) = \sum_{j=0}^{n_1} a_{1j} Z^j$, and $\widetilde{g}_2(Z) = \sum_{j=0}^{n_2} a_{2j} Z^j$ are truncated at orders n_0, n_1, and n_2. Notice that the ansatz in Eq. (20) has a slightly different structure from the traditional one [59]. Under Taylor expansions up to orders m_r and m_i, the functions χ_r and χ_i are

$$\chi_r(W) = \sum_{n=1}^{m_r} b_n W^n, \quad \chi_i(W) = \sum_{n=0}^{m_i} c_n W^n, \tag{22}$$

where b_1 and c_0 are set to 1 because they are redundant degrees of freedom after Eq. (22) is inserted into Eq. (21). Since m_i is set to zero in the following study, X will be approximated by a fitting ansatz g labeled by four indices (n_0, n_1, n_2, m_r). This ansatz is a function of L and w, or a two-dimensional surface embedded in a three-dimensional (L, w, X) space. The critical point w_c of the system satisfies the condition $dX(L, w_c)/dL = 0$. Geometrically, this point has the w value, along the curve specified by which the surface attitude is invariant of L.

III. RESULTS

A. Vibrational density of states of water

We carried out the molecular dynamics simulation on the FSPC/E water system introduced in Sec. II A and collected an ensemble of instantaneous molecule configurations, whose normal modes were calculated as discussed in Sec. II B. The INM DOS of the system is depicted by the black curve in Fig. 1. According to Eq. (8), this DOS can be partitioned into a translational DOS $D^{\text{trans}}(\omega)$, a rotational DOS $D^{\text{rot}}(\omega)$, and a stretching DOS $D^{\text{stretch}}(\omega)$, plotted by the pink dashed, orange dotted, and blue dash-dotted curves, respectively. While $D^{\text{trans}}(\omega)$ and $D^{\text{rot}}(\omega)$ dominate the low- and high-frequency regimes, respectively, $D^{\text{stretch}}(\omega)$ is significant only around the extremely high frequency of 3600 cm^{-1} for the O-H stretching. These features are consistent with those of the modified FSPC model [21] and the rigid SPC/E model [60], where the latter has only $D^{\text{trans}}(\omega)$ and $D^{\text{rot}}(\omega)$. The general evidence that the low- (high-) frequency modes are more extended (localized) indicates that the translational (rotational) modes are more extended (localized). It matches our intuition that the translational energy of a particle can be more easily handed on to its adjacent particles, in comparison with the rotational energy. The crossover of $D^{\text{trans}}(\omega)$ and $D^{\text{rot}}(\omega)$ of the unstable modes is located at $\text{Im}(\omega) \approx -160 \, \text{cm}^{-1}$, as shown in the inset of Fig. 1. This transition point is interestingly not far from the imaginary critical frequency $\text{Im}(\omega) \approx -131.6 \, \text{cm}^{-1}$ of the LDT calculated in Sec. III B.

B. Finite-size scaling of α_m

The first scaling quantity we employee to quantify the critical parameters of the FSPC/E water model is α_m, the position of the maximum of $P(\alpha)$. An indispensable procedure in this approach is measuring the local vibrational intensity α, which is conventionally counted on fixed boxes as described in Eq. (9). Such counting is, however, time consuming for

liquids because a series of judgements are required to decide in which boxes the molecules are located. To get rid of this complexity, we slightly modify the procedure and count α on mobile molecules. The $P(\alpha)$ constructed from box and molecule counts will be almost the same when the system size is large. Both convey the same message about how probable one can find intensity α in the system. After the complete atomic dynamics has been calculated by molecular dynamics simulations, the three atoms in the ith water molecule are coarse grained as a single particle with the vibrational strength

$$\mu_i = \sum_{\alpha=1}^{3} \sum_{\mu=x,y,z} |c_{i\alpha\mu}|^2, \qquad (23)$$

where $c_{i\alpha\mu}$ is as defined in Eq. (5). Physically, this coarse-graining procedure sets the lowest scale of the fractal structure of the vibrational wave provided it is a critical mode. Technically, it lifts some numerical errors caused by random noises [43]. Let ρ be the fluid density, L_{sys} be the system length as in Eq. (9), and m_{H} and m_{O} be the masses of hydrogen and oxygen atoms, respectively. Then $L = [\rho/(2m_{\text{H}} + m_{\text{O}})]^{1/3} L_{\text{sys}}$ is a dimensionless length of the system in units of the length of the water molecule, where $[\rho/(2m_{\text{H}} + m_{\text{O}})]^{-1}$ is the average volume of the molecule. Given the vibrational strength μ for a molecule, its rescaled intensity of local vibration is defined as

$$\alpha = -\ln\mu/\ln L. \qquad (24)$$

Although this intensity has the same form as the conventional Hölder exponent α in Eq. (9), it is counted on mobile molecules instead of fixed boxes.

Multifractal fluctuation is a hallmark of the critical modes at the LDT. This behavior is distinguished from those of the fully extended or localized modes away from the LDT. Figure 2 illustrates such fluctuation on a critical mode at $\text{Im}(\omega) = -130.25$, where the molecules vibrating with different intensities α are plotted in different colors and have different fractal dimensions. Therein, the molecules of $\alpha \approx 4.0$ colored in blue are the majority population. Here recall that $\text{Im}(\omega) = -130.25$ stands for the imaginary frequency $\omega = 130.25i$, according to the convention discussed in Sec. II B. Throughout this paper, the value of a quantity at frequency $\text{Im}(\omega)$ is referred to as the average value of this quantity over all modes within a narrow frequency observation window $\Sigma = [\text{Im}(\omega) - \Delta\omega/2, \text{Im}(\omega) + \Delta\omega/2]$ around $\text{Im}(\omega)$, with the window width $\Delta\omega = 1.2$ cm^{-1}. Accordingly, the histogram $\Delta N_\alpha/\bar{N}$ of α at frequency $\text{Im}(\omega)$ mentioned after Eq. (9) is constructed by counting the number of water molecules vibrating with α over all vibrational modes within Σ and over all collected water configurations. After normalization, this histogram will converge to the smooth PDF $P(\alpha)$, when the molecule number N in each configuration or the configuration number N_{conf} in the ensemble is large. If N_{eigen} denotes the number of eigenmodes within Σ over all configurations, $N_{\text{hist}} = N N_{\text{eigen}}$ is the number of α used to construct the above histogram at frequency $\text{Im}(\omega)$. Table I collects these data of numbers for plotting Figs. 3 and 4, where $\bar{N}_{\text{eigen}}$ is the average of the N_{eigen} over all frequency windows Σ of a given N.

Figure 3(a) depicts the $P(\alpha)$ of the FSPC/E model with $N = 18\,000$ at nine different frequencies $\text{Im}(\omega)$. While varying the frequency from $\text{Im}(\omega) = -110$ to -190 cm^{-1} with equal
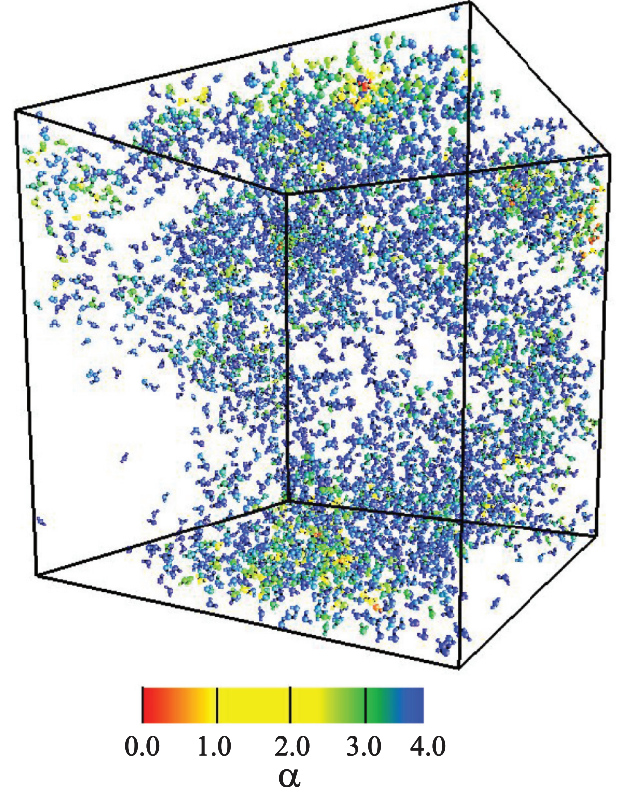

FIG. 2. (Color online) Snapshot of multifractal vibrations of $N = 18\,000$ water molecules at $\text{Im}(\omega) = -130.25$. The color of a water molecule represents the magnitude of the rescaled local vibrational intensity α on this molecule. In this plot, only molecules with sufficiently large vibrations $\alpha < 4.0$ are presented. The molecules of different colors have different fractal dimensions, which form the multifractal fluctuations of the critical mode.

distance 10 cm^{-1}, $P(\alpha)$ shifts rightward and α_m increases slightly. Besides the frequency dependence, $P(\alpha)$ and its α_m also vary with the molecule number N. However, Fig. 3(b) shows that at $\text{Im}(\omega) = -130.0$ cm^{-1} the value of α_m is insensitive to N, although the height $P(\alpha_m)$ still grows with the increasing N. This trend is the same as that observed in the 3D AM [41] and the TLJL [17] and that indicated in Eq. (15). Therefore, this $\text{Im}(\omega)$ value is already very close to the position of the size invariant α_m and the critical frequency. We can transform the $P(\alpha)$ of this $\text{Im}(\omega)$ into the fractal spectrum $f(\alpha)$ via Eq. (15). The black curve in Fig. 3(c) is the $f(\alpha)$ for $N = 18\,000$, which is almost the same as that for $N = 12\,000$. This curve agrees very well with the red curve, which is the

TABLE I. Data amounts used in the multifractal analysis. Here N water molecules are confined in a cubic box of dimensionless length L or of length L_{sys} in units of nm, N_{conf} is the number of water configurations, and $\bar{N}_{\text{eigen}}$ is the mean number of eigenmodes in a frequency window Σ.

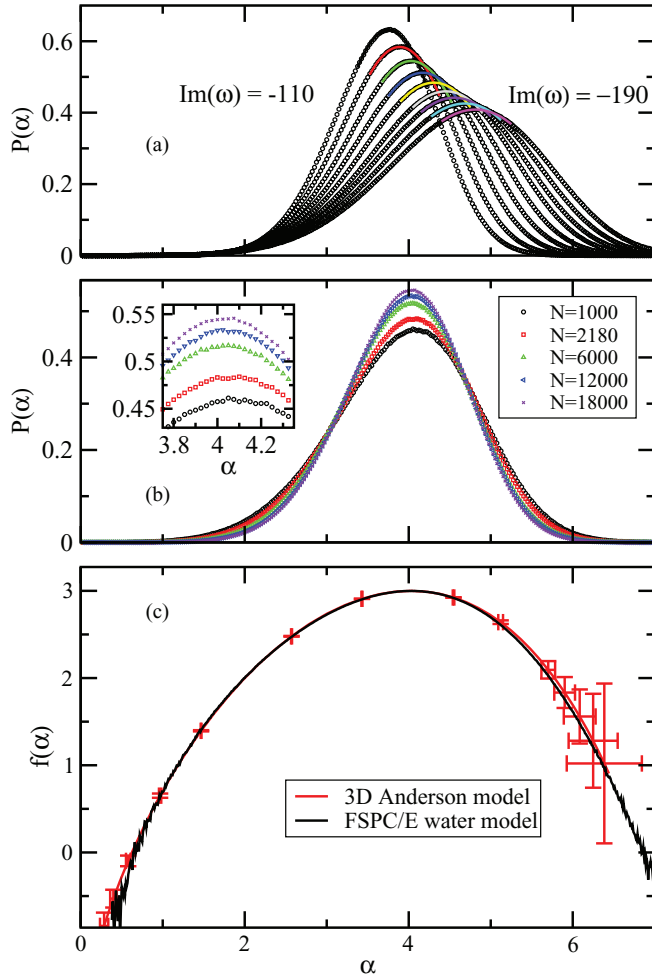| N	1000	2180	6000	12000	18000
N_{conf}	24193	5294	1690	1131	898
$\bar{N}_{\text{eigen}}$	29507	13780	9194	5334	4660
L_{sys} (nm)	3.104	4.025	5.641	7.107	8.136
L	10.0000	12.9664	18.1712	22.8943	26.2074

FIG. 3. (Color online) (a) Probability density functions $P(\alpha)$ of $N = 18\,000$ water molecules at nine frequencies between $\mathrm{Im}(\omega) = -110$ and -190. The top area of each $P(\alpha)$ is fitted by a third-order polynomial (solid curves). (b) The $P(\alpha)$ of various system sizes at $\mathrm{Im}(\omega) = -130$, where the top areas of these curves are magnified in the inset. (c) Multifractal spectrum $f(\alpha)$ at $\mathrm{Im}(\omega) = -130$. The black curve is the $f(\alpha)$ calculated from the $P(\alpha)$ of $N = 18\,000$ water molecules in the FSPC/E model. The red curve is the $f(\alpha)$ of the 3D AM [56].

FIG. 4. (Color online) (a) The α_m values at various $[N, \mathrm{Im}(\omega)]$ points are depicted at the centers of corresponding error bars. These α_m are fitted by a fitting surface (21) with $(n_0,n_1,n_2,m_r) = (4,4,3,3)$, which is projected onto five colored curves at five different N. The gray stripe is the area where the LDT occurs. In the inset, the scaling function (solid curve) is plotted from the data in the expansion $(n_0,n_1,n_2,m_r) = (4,4,3,3)$ in Table II. (b) Same as (a) except that α_m is replaced by $\tilde{\alpha}_0$ and the data of $(n_0,n_1,n_2,m_r) = (4,4,3,3)$ in Table II are replaced by the data of $(n_0,n_1,n_2,m_r) = (4,4,2,3)$ in Table III.

$f(\alpha)$ of the critical modes of the 3D AM [56]. This confirms the multifractal nature of the critical modes of the FSPC/E water model.

To pursue the exact critical frequency and exponent, it is crucial to know the accurate location of α_m. The PDFs in Figs. 3(a) and 3(b) are in reality normalized histograms. Although these functions look smooth, fluctuations still can be seen when they are magnified [inset of Fig. 3(b)]. Even this slight nonsmoothness can significantly affect the selection of α_m and subsequently the determination of the critical parameters, in particular, the critical exponent. To get rid of these numerical errors, let us first fit the top area of each $P(\alpha)$ by a third-order polynomial, as denoted by the colored curves in Fig. 3(a). The value of α_m is then the position of the maximum of the fitting polynomial. In Fig. 4(a), the α_m of 13 frequencies for $N = 18\,000$ are calculated and depicted at the centers of the 13 purple error bars. Following the same
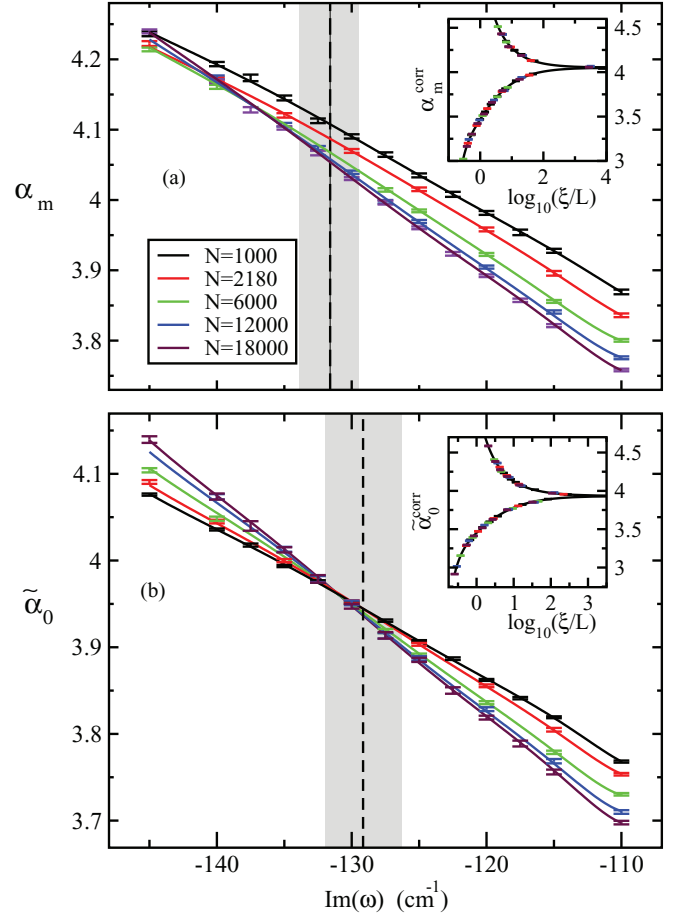
procedures, the α_m of four other system sizes $N = 1000, 2180, 6000,$ and $12\,000$ are also calculated. Here, for convenience, we have used the integer N to replace the noninteger L to denote the system size (see the relation between N and L in Table I). The α_m of these N are located at the centers of the black, red, green, and blue error bars in Fig. 4(a), respectively. To decide the widths of these error bars, recall that each α_m, which is the center of an error bar, is the position of the maximum of a $P(\alpha)$ generated by N_{hist} intensities α. If we randomly select only $N_{\mathrm{hist}}/3$ of these α to build up a less smooth $P(\alpha)$, its α_m will generally deviate from the α_m of the $P(\alpha)$ constructed from complete data. Repeating such random selections, the obtained α_m values will form a distribution $h(\alpha_m)$, which tends to a Gaussian function at large N_{hist}. The standard deviations of $h(\alpha_m)$ at different $[N,\mathrm{Im}(\omega)]$ are the error bars plotted in Fig. 4(a). If more than $N_{\mathrm{hist}}/3$ of α are selected, $h(\alpha_m)$ will be narrower and the error bar will be smaller. Since these error

TABLE II. Critical parameters estimated by the scaling of α_m. A surface ansatz of orders n_0, n_1, n_2, and m_r has N_p unknowns. It is used to fit N_d data points α_m within the upper and lower bounds of frequencies ω_{up} and ω_{low}, respectively. Here $\text{Im}(\omega_c)$ is the critical frequency, α_{mc} is the α_m at $\text{Im}(\omega_c)$, y is the irrelevant shift, ν is the critical exponent, χ^2 is the χ^2 statistics, and Q is the goodness of fit. The values in parentheses stand for the error bars obtained from 95% confidence intervals. All five fits are acceptable fits, among which the first one highlighted in bold is a stable fit.

n_0	n_1	n_2	m_r	N_p	$\text{Im}(\omega_{up})$	$\text{Im}(\omega_{low})$	N_d	α_{mc}		$\text{Im}(\omega_c)$		y		ν		χ^2	Q
4	**4**	**3**	**3**	19	−110	−145	50	4.04	(0.04)	−131.6	(2.2)	−1.36	(0.36)	1.60	(0.31)	42.9	0.08
5	4	3	3	20	−110	−145	50	4.03		−131.2		−1.68		1.53		44.0	0.05
5	5	3	3	21	−110	−145	50	4.05		−132.0		−1.68		1.45		38.7	0.11
4	4	4	3	20	−110	−145	50	4.04		−131.6		−1.50		1.68		43.3	0.06
4	4	3	4	20	−110	−145	50	4.03		−131.2		−1.68		1.53		44.0	0.05

bars can be artificially tuned, they have nothing to do with the efficiency of numerical calculations.

In Fig. 4(a), the α_m of each N are approximately located on a curve and the irrelevant shift of these curves is apparently seen. An extrapolation suggests that the critical frequency $\text{Im}(\omega_c)$ should be slightly larger than $\text{Im}(\omega) = -135$. Since the data points $[N, \text{Im}(\omega), \alpha_m]$ in Fig. 4(a) are close to that frequency, they can be fitted by the surface ansatz (21) truncated at (n_0, n_1, n_2, m_r). As an example, let us substitute the orders $(n_0, n_1, n_2, m_r) = (4,4,3,3)$ into Eq. (21) to fit these points. It yields the critical frequency $\text{Im}(\omega_c) = -131.6 \pm 2.2$, as well as $\alpha_{mc} = 4.04 \pm 0.04$, $y = -1.36 \pm 0.36$, and $\nu = 1.60 \pm 0.31$ (the row highlighted in bold in Table II), where α_{mc} is the α_m at $\text{Im}(\omega_c)$. These values are characteristics of the fitted surface and the solid curves in Fig. 4(a) are the curves projected from that surface at $N = 1000$, 2180, 6000, 12 000, and 18 000. To determine the error bars of $[\alpha_{mc}, \text{Im}(\omega_c), y, \nu]$ in Table II, we randomly synthesize around 1000 copies of α_m at each $[N, \text{Im}(\omega)]$, following the probability distribution $h(\alpha_m)$ constructed in Fig. 4(a). This generates 1000 synthesized surfaces of α_m and then 1000 sets of fitted parameters $[\alpha_{mc}, \text{Im}(\omega_c), y, \nu]$, which are collected to form histograms $h_1(\alpha_{mc})$, $h_2[\text{Im}(\omega_c)]$, $h_3(\nu)$, and $h_4(y)$ of α_{mc}, $\text{Im}(\omega_c)$, ν, and y, respectively. The 95% confidence intervals of these histograms are the error bars of the corresponding parameters for $(n_0, n_1, n_2, m_r) = (4,4,3,3)$ in Table II.

The orders $(n_0, n_1, n_2, m_r) = (4,4,3,3)$ specify a fit ansatz, which is one among infinitely many possible choices. An ansatz is used to fit the numerical raw data α_m, which usually contain inevitable slight deviations from their real values. Enhancing the orders (n_0, n_1, n_2, m_r) does not guarantee a better fit because it might magnify local numerical errors and predict less smooth surfaces. The set of orders $(n_0, n_1, n_2, m_r) = (4,4,3,3)$ is regarded as a good fit because it conforms to the following selection principles. (i) Only the α_m data within a small range $[\text{Im}(\omega_{low}), \text{Im}(\omega_{up})]$ around $\text{Im}(\omega_c)$ are used for scaling studies since the scaling formula (21) is an expansion with respect to $\text{Im}(\omega_c)$. (ii) In such a small range, the real α_m surface is supposed to vary slowly with $[N, \text{Im}(\omega)]$ and thus its fitting surface should have low orders (n_0, n_1, n_2, m_r). (iii) A fit is rejected when its goodness, Q factor, is smaller than 0.01, where the χ^2 statistics of the data points is minimized by the downhill simplex method [61]. (iv) If the y of an expansion

lies outside the region $-2.0 < y < -1.0$, this expansion is not regarded as reasonable. (v) The fit should be so stable that it does not change significantly when the expansion orders are increased. [43]. While all rows in Table II are acceptable fits satisfying principles (i)–(iv), the first one (4,4,3,3) fulfills the additional stability condition of principle (v). Notice that to test the stability of (4,4,3,3) the original third row of Table II should be (4,5,3,3), which, however, is not a good expansion because it violates the convention $n_0 \geqslant n_1 \geqslant n_2$. Thus we use the next neighboring expansion (5,5,3,3) for the stability test.

Owing to Eq. (21), one can subtract the irrelevant effect in α_m and explore the corrected intensity[2]

$$\alpha_m^{\text{corr}} = \alpha_m + \widetilde{g}_0(\chi_r L^{1/\nu}). \quad (25)$$

Taking α_m^{corr} as the perpendicular axis and $\log_{10}(\xi/L)$ with $\xi = |\chi_r|^{-\nu}$ as the horizontal axis, one obtains a scaling function with two sheets. As an example, the solid curve in the inset of Fig. 4(a) is the scaling function obtained from the parameters of (4,4,3,3) in Table II with $N = 18\,000$. The upper sheet represents the localized modes, whereas the lower sheet corresponds to the extended modes. All α_m points on the five curves in Fig. 4(a) collapse perfectly onto this scaling function, which confirms the efficiency of the scaling process.

C. Finite-size scaling of $\widetilde{\alpha}_0$

In the second approach, we use the same INM data, but calculate their singularity strength $\widetilde{\alpha}_q$ at $q = 0$ and take it as a scaling quantity. Figure 4(b) depicts several $\widetilde{\alpha}_0$ at different $[N, \text{Im}(\omega)]$. We repeat the same fitting procedure following the above selection principles (i)–(iv), where $-2.0 < y < -1.0$ in (iv) has been replaced by $-2.5 < y < -1.0$ and $\widetilde{\alpha}_0 > 3.90$. It yields the five acceptable fits in Table III, where the last four are neighboring expansions of the first one and are constrained by the ordering $n_0 \geqslant n_1 \geqslant n_2$, with the same reason as for constructing Table II. According to principle (v), the first fit is a stable fit, which has $\text{Im}(\omega_c) = -129.2 \pm 2.9$,

---

[2]For $X = g_0 + g_1/\ln \lambda$ with a fixed λ, one can define $X^{\text{corr}} \equiv X - g_1/\ln \lambda = g_0$ to eliminate the irrelevant effect. For $X = X_0 + (g_0 + g_1 + g_2)/\ln L$ with a varying L, one can instead consider $X^{\text{corr}} \equiv (X - X_0)\ln L - g_1 - g_2 + X_0 = g_0 + X_0$.

TABLE III. Critical parameters estimated by the scaling of $\widetilde{\alpha}_0$. All notations are the same as those in Table II and $\widetilde{\alpha}_{0c}$ is the $\widetilde{\alpha}_0$ at $\mathrm{Im}(\omega_c)$.

n_0	n_1	n_2	m_r	N_p	$\mathrm{Im}(\omega_{\mathrm{up}})$	$\mathrm{Im}(\omega_{\mathrm{low}})$	N_d	$\widetilde{\alpha}_{0c}$		$\mathrm{Im}(\omega_c)$		y		ν		χ^2	Q
4	**4**	**2**	**3**	18	−110	−145	50	3.93	(0.06)	−129.2	(2.9)	−1.84	(0.69)	1.57	(0.34)	42.08	0.11
4	4	2	4	19	−110	−145	50	3.90		−127.1		−1.86		1.51		39.73	0.14
4	4	3	3	19	−110	−145	50	3.92		−128.2		−1.76		1.59		40.43	0.12
5	5	2	3	20	−110	−145	50	3.92		−128.0		−1.50		1.53		45.33	0.04
5	4	2	3	19	−110	−145	50	3.95		−130.3		−1.52		1.27		48.23	0.03

$\widetilde{\alpha}_{0c} = 3.93 \pm 0.06$, $y = -1.84 \pm 0.69$, and $\nu = 1.57 \pm 0.34$. In analogy to the inset of Fig. 4(a), all points on the five $\widetilde{\alpha}_0$ curves in Fig. 4(b) collapse perfectly onto their corresponding scaling function $\widetilde{\alpha}_0^{\mathrm{corr}}$ in the inset of Fig. 4(b), where $N = 18\,000$ and the parameters of (4,4,2,3) in Table III are used.

With the results from α_m and $\widetilde{\alpha}_0$ scalings, we are able to discuss the accuracies of these approaches. At first glance, one might expect a higher accuracy from $\widetilde{\alpha}_0$, as the crossing points in Fig. 4(b) are more densely clustered than those of α_m in Fig. 4(a). Nevertheless, a comparison shows that $\widetilde{\alpha}_0$ scaling is less precise due to the less apparent peak structure of histograms h_1, h_2, h_3, and h_4, more unreasonable fits eliminated by principle (iv), and less acceptable fits obeying principles (i)–(iv). As a result, the parameters $[\widetilde{\alpha}_{0c}, \mathrm{Im}(\omega_c), y, \nu]$ fitted by $\widetilde{\alpha}_0$ deviate slightly from those obtained by α_m and those known in the 3D AM. Naively, one might conclude that α_m is a better scaling quantity than $\widetilde{\alpha}_0$, which is, however, unfair. To clarify this point, suppose we need to fit some experimentally measured data points to predict a curve described by $Y(x) = c_0 + c_1 x + c_2 x^2$. If these points accumulate near $x = 0$, they can well reveal the local linear behavior of $Y(x)$ around 0, but fail to predict the precise nonlinear behavior described by c_2, as long as the points have slight errors. For a general function $Y(x)$, the most ideal data points are those that are densely (sparsely) distributed in the fast (slowly) varying area of $Y(x)$. The irrelevant exponent y studied above describes the X surface in Eq. (20) outside the point $L = \infty$ and plays a similar role as c_2. For our α_m and $\widetilde{\alpha}_0$ data, the selected system sizes are not yet sufficiently ideal since the crossing points are too dispersed in Fig. 4(a) and too localized in Fig. 4(b). Surprisingly, the strong irrelevant shift in Fig. 4(a) still can be efficiently described by the irrelevant scaling variable, as one can see that the LDT area (gray stripe) are outside most crossing points. It offers a good example demonstrating the potential of the scaling procedure. In contrast, the densely localized crossing points in Fig. 4(b) make it difficult to extract the precise value of y and other fit parameters related to it, which is plausible from the above c_2 example. As a whole, if the system sizes for α_m and $\widetilde{\alpha}_0$ are individually properly selected, the scaling efficiencies of these two quantities should be equally good. If they are not properly selected, the precision of the fitted parameters cannot be considerably improved by enlarging the system ensemble or changing fitting conditions. Properly selected system sizes seem to be a rather crucial factor for reducing the error bars of fit parameters, in particular, that of ν.

A further comparison shows that the distinct patterns in Figs. 4(a) and 4(b) imply that the mean $\widetilde{\alpha}_0$ and the position of the maximum α_m of $P(\alpha)$ do not coincide with each other. Indeed, the $P(\alpha)$ of a finite system is generally slightly asymmetric with respect to the position of its maximum. This asymmetry has been observed in the AM [42] and the TLJL [17] and can also be observed in Fig. 3(b) of the current FSPC/E model. In spite of that, numerical studies in the AM have shown that $\widetilde{\alpha}_0$ will approach α_m at $\lambda \to 0$ [42]. Thus the patterns in Figs. 4(a) and 4(b) will likely converge to each other in the thermodynamic limit. Close to that limit, irrelevant behavior is insignificant and both $\widetilde{\alpha}_0$ and α_m scalings should be equally efficient. Notice that whether a system size is sufficiently close to the thermodynamics limit depends, in some sense, on the quantities defined in the INMs. While the pattern of α_m in Fig. 4(a) looks far from that limit, that of $\widetilde{\alpha}_0$ in Fig. 4(b) seems to be comparatively close to it.

IV. DISCUSSION

Our simulations of up to 54 000 atoms on the FSPC/E water model predict the critical frequency of the unstable INM at $\mathrm{Im}(\omega_c) = -131.6 \pm 2.2$, which is rather robust against the change of fitting conditions. In contrast, the critical exponent $\nu = 1.60 \pm 0.31$ is more sensitive to those conditions and has larger relative error bars. However, the calculated ν value still lies close to those of other calculated systems. For instance, $\nu = 1.4^{+0.15}_{-0.15}$ [34], $\nu = 1.45^{+0.2}_{-0.2}$ [35], $\nu = 1.58^{+0.03}_{-0.03}$ [42], $\nu = 1.59^{+0.012}_{-0.011}$ [43], and $\nu = 1.57^{+0.02}_{-0.02}$ [45] for the 3D AM, $\nu = 1.61^{+0.07}_{-0.06}$ for electrons with topological disorder [62], $\nu = 1.55^{+0.002}_{-0.002}$ for disordered phonons [63], $\nu \approx 1.5$–1.6 for electrons in fcc and bcc lattices [64], $\nu = 1.550^{+0.020}_{-0.017}$ [14] and $\nu \approx 1.57$–1.59 [15] for phonons in the DLMS of various disorder distributions, $\nu_p = 1.55^{+0.09}_{-0.09}$ for the real and $\nu_n = 1.60^{+0.07}_{-0.07}$ for the imaginary INMs of the TLJL [36], and $\nu = 1.63^{+0.05}_{-0.05}$ [65] and $\nu = 1.59^{+0.01}_{-0.01}$ [47] for the experimentally and numerically studied QARs, respectively. All these systems belong to the symmetry class of spinless time-reversal invariant 3D systems in the random matrix theory [5] and are expected to have a universal ν at the LDT. It is widely accepted that this ν should be close to 1.6. In spite of the slight deviations from one another in the above-reported ν, they are readily distinguishable from $\nu = 2.593^{+0.05}_{-0.06}$ for the class of integer quantum Hall effect [66].

Besides the current FSPC/E, there exists another liquid, the TLJL simple fluid, whose LDT behaviors have been investigated. The critical properties in that system were quantified by scaling the second moment of the nearest-neighbor level

spacing distributions [36] and the multifractal properties of their critical INMs were discussed in Ref. [17]. A comparison between Fig. 2(b) in the current study and Fig. 2 of Ref. [36] shows that the INM DOS of FSPC/E contains much richer features than that of TLJL, even after the ω axis of the former plot is unified with the λ axis of the latter plot. Some of the features in the FSPC/E arise from local motions, such as the stretching motion of O-H bond. It generates a prominent peak at around 3500–3750 cm^{-1} in the real frequency branch, which is absent in the INM DOS of TLJL. Additionally, the rotation of a nonisotropic FSPC/E molecule can affect the translational motions of its surrounding molecules and be another reason for the difference between the INM DOS of the FSPC/E and TLJL. However, the main difference appears in the DOS of stable INMs and that of unstable INMs is similar in the FSPC/E, the TLJL, and the liquid N-methylacetamide dimer we are studying. This similarity raises the question of whether a broad range of liquids has around the same Im(ω_c) close to -130 cm^{-1}. In addition, it is unknown whether the coincidence of ν in the real and imaginary frequency branches of the TLJL [17] still holds in the FSPC/E. Moreover, it is unclear whether the close distance between the locations of the LDT and the translational transition in the unstable INMs of FSPC/E is valid in its stable INMs and other liquids.

The value $\nu \approx 1.6$ is widely accepted for systems of the 3D orthogonal class. However, in the example of the 3D AM, this value is correct only when the disorder of the system is uncorrelated or weakly correlated. If the disorder is strongly correlated, ν may vary continuously with the disorder correlation strength. For instance, if the disorder follows the scale-free correlation function decaying in space asymptotically as $g(r) = r^{-a}$, the extended Harris criterion [67,68] tells us that there exists a critical value a_c such that $\nu = \nu_0$ for $a > a_c$ and $\nu = 2/a$ for $a < a_c$, where ν_0 is the critical exponent of uncorrelated disorder. In liquids, an instantaneous configuration of particles corresponds to a random disorder configuration in the AM. Such a comparison leads to several puzzling questions: Do liquids have a corresponding $g(r)$ describing their disorder correlation? If yes, how is this $g(r)$ related to the interparticle interaction of liquids and are the $g(r)$ for the TLJL and FSPC/E the same? Does there exist some critical value a_c in liquids, beyond which ν deviates from ν_0? If yes, is the a of the FSPC/E under or above a_c? Probably it is more rigorous to clarify these questions before expecting water to have exactly the same ν as that of the 3D AM.

V. CONCLUSION

Water plays an essential role in nature. While several physical properties of this system have been extensively investigated, its critical and multifractal behaviors of vibrations are rarely quantitatively discussed. In this work we demonstrated the multifractal behaviors of the FSPC/E water model through the multifractal fluctuations in Fig. 2, the PDF $P(\alpha)$ of the local Hölder exponent α in Fig. 3(b), and the multifractal dimension $f(\alpha)$ in Fig. 3(c). Based on the multifractal and the size invariant properties of the LDT, we quantified several critical parameters of the FSPC/E, including the critical frequency of the unstable INM at Im(ω_c) ≈ -131.6 cm^{-1}, the critical exponent at $\nu \approx 1.60$, the irrelevant exponent at $y \approx -1.36$, and the maximum position of the local Hölder exponent at $\alpha_{mc} \approx 4.04$ (see Table II and III for more precise values). While several methods have been employed to calculate the critical point of the 3D AM, no method was used to evaluate that of water before. The precise critical value extracted in this work is crucial for discussing the critical, multifrcatal, and diffusion properties of liquid water, as mentioned in Sec. I. The calculated ν of the SPC/E is close to the expected value $\nu \approx 1.6$ for the 3D orthogonal class in the Wigner-Dyson classification. Since the α_{mc} and $f(\alpha)$ of the SPC/E coincide with those of the 3D AM and TLJL, they might be universal for more general wave systems and could serve as additional criteria for determining their LDT positions. The current results raise several open questions, which are discussed in Sec. IV. In summary, this work (i) quantified the critical vibrational frequency of liquid water, beyond conventional solid samples, (ii) provided a soft matter system with an explicitly calculated ν in the 3D orthogonal class, and (iii) validated the applicability of the multifractal scaling concept beyond Andersonian systems.

[1] P. W. Anderson, Phys. Rev. **109**, 1492 (1958).

[2] A. Lagendijk, B. van Tiggelen, and D. S. Wiersma, Phys. Today **62** (8), 24 (2009).

[3] B. Kramer and A. MacKinnon, Rep. Prog. Phys. **56**, 1469 (1993).

[4] M. Janssen, Phys. Rep. **295**, 1 (1998).

[5] F. Evers and A. D. Mirlin, Rev. Mod. Phys. **80**, 1355 (2008).

[6] *Scattering and Localization of Classical Waves in Random Media*, edited by P. Sheng (World Scientific, Hackensack, NJ, 1990).

[7] S. John, Phys. Rev. Lett. **58**, 2486 (1987).

[8] J. Gómez Rivas, R. Sprik, A. Langendijk, L. D. Noordam, and C. W. Rella, Phys. Rev. E **62**, R4540 (2000).

[9] M. Störzer, P. Gross, C. M. Aegerter, and G. Maret, Phys. Rev. Lett. **96**, 063904 (2006).

[10] J. J. Ludlam, S. N. Taraskin, and S. R. Elliott, Phys. Rev. B **67**, 132203 (2003).

[11] J. J. Ludlam, S. N. Taraskin, S. R. Elliott, and D. A. Drabold, J. Phys.: Condens. Matter **17**, L321 (2005).

[12] S. D. Bembenek and B. B. Laird, Phys. Rev. Lett. **74**, 936 (1995).

[13] H. Hu, A. Strybulevych, J. H. Page, S. E. Skipetrov, and B. van Tiggelen, Nat. Phys. **4**, 945 (2008).

[14] S. D. Pinski, W. Schirmacher, T. Whall, and R. A. Römer, J. Phys.: Condens. Matter **24**, 405401 (2012).

[15] S. D. Pinski, W. Schirmacher, and R. A. Römer, Europhys. Lett. **97**, 16007 (2012).

[16] V. Pouthier and C. Falvo, Phys. Rev. E **69**, 041906 (2004).

[17] B. J. Huang and T. M. Wu, Phys. Rev. E **82**, 051133 (2010).

[18] B. J. Huang and T. M. Wu, Comput. Phys. Commun. **182**, 213 (2011).

[19] V. Clapa, T. Kottos, and F. W. Starr, J. Chem. Phys. **136**, 144504 (2012).

[20] M. Cho, G. R. Fleming, S. Saito, I. Ohmine, and R. M. Stratt, J. Chem. Phys. **100**, 6672 (1994).

[21] H. Ahlborn, X. Ji, B. Space, and P. B. Moore, J. Chem. Phys. **111**, 10622 (1999).

[22] H. Torii, J. Phys. Chem. A **110**, 9469 (2006).

[23] F. Sciortino and P. Tartaglia, Phys. Rev. Lett. **78**, 2385 (1997).

[24] R. L. Murry, J. T. Fourkas, and T. Keyes, J. Chem. Phys. **109**, 2814 (1998).

[25] E. La Nave, A. Scala, F. W. Starr, F. Sciortino, and H. E. Stanley, Phys. Rev. Lett. **84**, 4605 (2000).

[26] W.-X. Li and T. Keyes, J. Chem. Phys. **111**, 5503 (1999).

[27] G. Seeley and T. Keyes, J. Chem. Phys. **91**, 5581 (1989).

[28] B. Madan, T. Keyes, and G. Seeley, J. Chem. Phys. **92**, 7565 (1990).

[29] B. Madan, T. Keyes, and G. Seeley, J. Chem. Phys. **94**, 6762 (1991).

[30] P. Moore and T. Keyes, J. Chern. Phys. **100**, 6709 (1994).

[31] J. Daniel Gezelter, E. Rabani, and B. J. Berne, J. Chem. Phys. **107**, 4618 (1997).

[32] T. Keyes, W.-X. Li, and U. Zurcher, J. Chem. Phys. **109**, 4693 (1998).

[33] J. D. Gezelter, E. Rabani, and B. J. Berne, J. Chem. Phys. **109**, 4695 (1998).

[34] I. Kh. Zharekeshev and B. Kramer, Phys. Rev. Lett. **79**, 717 (1997).

[35] F. Milde, R. A. Römer, and M. Schreiber, Phys. Rev. B **55**, 9463 (1997).

[36] B. J. Huang and T. M. Wu, Phys. Rev. E **79**, 041105 (2009).

[37] T. Nakayama and K. Yakubo, *Fractal Concepts in Condensed Matter Physics* (Springer, Berlin, 2003).

[38] J. Feder, *Fractals* (Plenum, New York, 1988).

[39] B. Mandelbrot, *The Fractal Geometry of Nature* (Freeman, New York, 1982).

[40] H. Aoki, J. Phys. C **16**, L205 (1983); Phys. Rev. B **33**, 7310 (1986).

[41] A. Rodriguez, L. J. Vasquez, and R. A. Römer, Phys. Rev. Lett. **102**, 106406 (2009).

[42] A. Rodriguez, L. J. Vasquez, K. Slevin, and R. A. Römer, Phys. Rev. Lett. **105**, 046403 (2010).

[43] A. Rodriguez, L. J. Vasquez, K. Slevin, and R. A. Römer, Phys. Rev. B **84**, 134209 (2011).

[44] M. L. Ndawana, R. A. Römer, and M. Schreiber, Eur. Phys. J. B **27**, 399 (2002).

[45] K. Slevin and T. Ohtsuki, Phys. Rev. Lett. **82**, 382 (1999).

[46] M. E. Parker and D. M. Heyes, J. Chem. Phys. **108**, 9039 (1998).

[47] G. Lemarié, B. Grémaud, and D. Delande, Europhys. Lett. **87**, 37007 (2009).

[48] D. van der Spoel *et al*., GROMACS User Manual version 4.5, 2010, www.gromacs.org.

[49] Y. Wu, H. L. Tepper, and G. A. Voth, J. Chem. Phys. **124**, 024503 (2006).

[50] T. Keyes, J. Phys. Chem. A **101**, 2921 (1997).

[51] M. Bollhöfer and Y. Notay, Comput. Phys. Commun. **177**, 951 (2007).

[52] M. Buchner, B. M. Ladanyi, and R. M. Stratt, J. Chem. Phys. **97**, 8522 (1992).

[53] A. D. Mirlin, Y. V. Fyodorov, A. Mildenberger, and F. Evers, Phys. Rev. Lett. **97**, 046803 (2006).

[54] I. A. Gruzberg, A. W. W. Ludwig, A. D. Mirlin, and M. R. Zirnbauer, Phys. Rev. Lett. **107**, 086403 (2011).

[55] L. J. Vasquez, A. Rodriguez, and R. A. Römer, Phys. Rev. B **78**, 195106 (2008).

[56] A. Rodriguez, L. J. Vasquez, and R. A. Römer, Phys. Rev. B **78**, 195107 (2008).

[57] H. Grussbach and M. Schreiber, Phys. Rev. B **51**, 663 (1995).

[58] E. Abrahams, P. W. Anderson, D. C. Licciardello, and T. V. Ramakrishnan, Phys. Rev. Lett. **42**, 673 (1979).

[59] L. J. Vasquez, K. Slevin, A. Rodriguez, and R. A. Römer, Ann. Phys. (Berlin) **18**, 901 (2009).

[60] S. L. Chang and T.-M. Wu, J. Chem. Phys. **121**, 3605 (2004).

[61] W. H. Press, B. P. Flannery, S. A. Teukolsky, and W. T. Vetterling, *Numerical Recipes in C: The Art of Scientific Computing* (Cambridge University Press, New York, 2007), Chap. 15.

[62] J. J. Krich and A. Aspuru-Guzik, Phys. Rev. Lett. **106**, 156405 (2011).

[63] S. D. Pinski and R. A. Römer, J. Phys. Conf. Ser. **286**, 012025 (2011).

[64] A. Eilmes, A. M. Fischer, and R. A. Römer, Phys. Rev. B **77**, 245117 (2008).

[65] M. Lopez, J.-F. Clément, P. Szriftgiser, J. C. Garreau, and D. Delande, Phys. Rev. Lett. **108**, 095701 (2012).

[66] K. Slevin and T. Ohtsuki, Phys. Rev. B **80**, 041304(R) (2009).

[67] A. Weinrib and B. I. Halperin, Phys. Rev. B **27**, 413 (1983).

[68] A. Weinrib, Phys. Rev. B **29**, 387 (1984).